NACA

RESEARCH MEMORANDUM

for the

Bureau of Aeronautics, Department of the Navy

FLIGHT TEST OF THE LATERAL STABILITY OF A 0.133-SCALE MODEL OF THE CONVAIR XFY-1 AIRPLANE WITH WINDMILLING PROPELLERS AT MACH NUMBERS FROM 0.70 TO 1.12

TED NO. NACA DE 369

By James A. Hollinger and Grady L. Mitcham

Langley Aeronautical Laboratory
Langley Field, Va.

NATIONAL ADVISORY COMMITTEE
FOR AERONAUTICS

WASHINGTON

NOV 9 1955

CONFIDENTIAL

NATIONAL ADVISORY COMMITTEE FOR AERONAUTICS

RESEARCH MEMORANDUM

for the

Bureau of Aeronautics, Department of the Navy

FLIGHT TEST OF THE LATERAL STABILITY OF A 0.133-SCALE MODEL OF THE CONVAIR XFY-1 AIRPLANE WITH WINDMILLING PROPELLERS AT MACH NUMBERS FROM 0.70 TO 1.12

TED NO. NACA DE 369

By James A. Hollinger and Grady L. Mitcham

SUMMARY

A flight test of a rocket-propelled model of the Convair XFY-1 airplane was conducted to determine the lateral stability and control characteristics. The 0.133-scale model had windmilling propellers for this test, which covered a Mach number range of 0.70 to 1.12. The center of gravity was located at 13.9 percent of the mean aerodynamic chord.

The methods of analysis included both a solution by vector diagrams and simple one- and two-degree-of-freedom methods.

The model was both statically and dynamically stable throughout the speed range of the test. The roll damping was good, and the slope of the side-force curve varied little with speed. The rudder was effective throughout the test speed range, although it was reduced to about 43 percent of its subsonic value at supersonic speeds.

INTRODUCTION

Rocket-model tests of the Convair XFY-1 airplane have been conducted by the Langley Pilotless Aircraft Research Division at the request of the Bureau of Aeronautics, Department of the Navy. The purpose of this program was to determine the effects of windmilling propellers on the lateral and longitudinal stability of the Convair XFY-1 (phase III) airplane at transonic speeds.

The XFY-1 is a modified-delta-wing airplane designed for vertical take-off and horizontal flight and is powered by an Allison T40 gas-turbine engine driving a dual-rotating, high-speed Curtiss propeller. Longitudinal control is achieved by two control surfaces acting as elevators, and roll control is achieved by the same surfaces acting differentially as ailerons. Rudders mounted at the trailing edge of both vertical tails give directional control.

This paper presents the results from the third in a series of tests. Results from the two previous tests, determination of some of the longitudinal-stability characteristics, are presented in reference 1 for a model without propellers, and in reference 2 for a model with windmilling propellers. The results presented and discussed herein were obtained from a lateral stability flight test of a 0.133-scale rocket-powered model of the XFY-1 with windmilling propellers. Data presented in reference 3 for a configuration with similar operating characteristics show that windmilling propellers have more effect upon the stability data than does the addition of power in the speed range covered by these tests. The lateral-stability characteristics were determined from an analysis of the transient motion induced by abrupt movement of the rudder.

SYMBOLS

a	total damping factor (logarithmic decrement of transient oscillation)
b	wing span, ft
c_P	propeller chord
D	diameter of propeller disc
h	propeller blade thickness
I_X	moment of inertia about body roll axis, slug-ft^2
I_Y	moment of inertia about body pitch axis, slug-ft^2
I_Z	moment of inertia about body yaw axis, slug-ft^2
I_{XZ}	product of inertia, slug-ft^2
m	mass of model, slugs

p	rolling angular velocity, radians/sec
q	dynamic pressure, lb/sq ft
R	Reynolds number
r	yawing angular velocity, radians/sec
S	wing area including body intercept, sq ft
$t_{0.5}$	time required for mean roll rate to approach halfway to final value, sec
V	velocity, ft/sec
W	model weight, lb
w	mass flow through duct, slugs/sec
α	angle of attack at model center of gravity, deg
β	angle of sideslip at model center of gravity, deg
β_p	propeller blade angle
δ	control deflection, deg
θ	angle of pitch, deg
ϕ	angle of roll, deg
Ω_p	phase angle of $\dot{\phi}$ relative to β, radians
ω	undamped circular frequency, radians/sec
ψ	angle of yaw, deg
C_h	hinge-moment coefficient
$c_{l,i}$	section design lift coefficient of propeller blade
C_l	rolling-moment coefficient
C_n	yawing-moment coefficient

C_{h_δ} hinge-moment parameter, $\frac{\partial C_h}{\partial \delta}$, deg

C_{l_p} damping-in-roll derivative, $\frac{\partial C_l}{\partial\left(\frac{pb}{2V}\right)}$

C_{l_r} coefficient of rolling moment due to yawing velocity, $\frac{\partial C_l}{\partial\left(\frac{rb}{2V}\right)}$

C_{l_β} coefficient of rolling moment due to sideslip, $\frac{\partial C_l}{\partial \beta}$, per radian

$C_{l_{\dot{\beta}}}$ coefficient of rolling moment due to sideslipping velocity, $\frac{\partial C_l}{\partial\left(\frac{\dot{\beta} d}{2V}\right)}$, per radian

C_{l_δ} control rolling-moment effectiveness coefficient, $\frac{\partial C_l}{\partial \delta}$

C_{n_p} coefficient of yawing moment due to rolling velocity, $\frac{\partial C_n}{\partial\left(\frac{pb}{2V}\right)}$

C_{n_r} coefficient of yawing moment due to yawing velocity, $\frac{\partial C_n}{\partial\left(\frac{rb}{2V}\right)}$

C_{n_β} coefficient of yawing moment due to sideslip, $\frac{\partial C_n}{\partial \beta}$, per radian

$C_{n_{\dot{\beta}}}$ coefficient of yawing moment due to sideslipping velocity, $\frac{\partial C_n}{\partial\left(\frac{\dot{\beta} b}{2V}\right)}$, per radian

[redacted]

C_{n_δ} control yawing-moment effectiveness coefficient, $\frac{\partial C_n}{\partial \delta}$, deg

C_{Y_β} coefficient of lateral force due to sideslip, $\frac{\partial C_Y}{\partial \beta}$

a_t/g lateral load factor as indicated by accelerometer at center of gravity

r_P/R_P fraction of tip radius

$\frac{\Delta C_h}{\Delta \delta}$ total hinge-moment parameter

The symbol $|j|$ represents the absolute magnitude of j and is always taken to be positive.

A dot over a symbol indicates that the variable has been differentiated with respect to time. Two dots indicate the second derivative.

MODEL

A three-view drawing of the model tested in this investigation is shown in figure 1; photographs of the model are presented in figure 2; and the physical characteristics of the model are given in table I. Figure 3 presents the propeller-section characteristics as a function of blade station.

The dual-rotating propeller had six Curtiss 1058-1059-XC-4 blades with an NACA 65-series airfoil section. For this test the propeller blade angle was 55° at the three-quarter radius. The spinners were made of aluminum alloy and rotated independently of each other on bearings located inside the model on a tachometer and on the sting.

Lateral control was provided by a pneumatic system operating two 6° swept, constant-chord, partial-span rudders at the trailing edge of the vertical fins. The rudders were deflected between angles of 0.2° and 3.8° in an approximate square wave during the time that the model decelerated in free flight. The elevons were preset at 3°, trailing edge up.

The wings and vertical tails had modified delta plan forms with NACA 63-009 airfoil sections. The wing had a 57° swept leading edge and an aspect ratio of 1.85. Gun pods and landing struts were located at the wing tips and landing struts were located on the vertical fins. Both wings and vertical fins were made of aluminum-alloy plates and spars built up to the proper contour with laminated mahogany.

A choking section (determined by the minimum cross-sectional area of the duct) and integrating total pressure pickup were installed in the duct exit in order to determine values of internal flow at Mach numbers above 1.0. Since the base of the model was the same as that of reference 1, no base pressure survey was made of this model.

INSTRUMENTATION

A telemeter system was used to record the lateral stability and drag data. Twelve channels of information were recorded simultaneously and continuously in order to obtain the data presented herein. The channels were: angle of attack; angle of sideslip; rate of roll; accelerations in the longitudinal, transverse, and normal directions at the center of gravity; accelerations in the transverse direction at the tail, rudder control position and hinge moment, free stream and duct exit total pressures, and propeller rotational speed.

A radiosonde, released at the time of firing, enabled the recording of free-stream temperature and static pressure over the altitude range covered by the test. The velocity and position in space of the model were determined by a CW Doppler radar and a radar tracking unit.

TESTS

The propeller and spinner rotate around the sting supporting the angle-of-attack vane, and precautionary measures were taken to minimize the bending in the sting which this rotation caused. The spinner, propeller, and tachometer assembly was mass balanced and dynamically balanced. The bearings were specially refitted to aid the rotating masses to run true around the sting. The superimposed vibration of the recording traces at the propeller rotational frequency was faired out before data reduction.

Ground tests indicated that it would not be necessary to apply flexibility corrections to the recorded rudder deflections.

The model was shaken by an electromagnetic shaker to determine the principal modes in which the model would distort. These modes are recorded in the following table:

Mode	Frequency, cps	Sketch
Fuselage bending	52	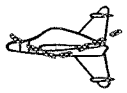
Wing-fuselage bending	152	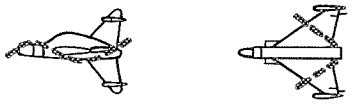
Wing second bending	237	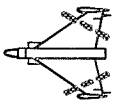
Wing torsion	345	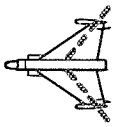

The model was flight tested at the Pilotless Aircraft Research Station at Wallops Island, Va. It was boosted from a zero-length launcher with a 6.25-inch-diameter Deacon rocket motor. The booster burned out at a low supersonic speed and separated at approximately 3.16 seconds from the model, which was allowed to coast freely. The data presented herein were obtained during the coasting phase. Figure 2(b) is a photograph of the model-booster combination prior to launching.

ACCURACY

The estimated maximum errors in the basic quantities used to determine the lateral stability derivatives C_{Y_β}, C_{n_β}, C_{l_β}, C_{l_r}, and $C_{n_r} - C_{n_{\dot{\beta}}}$ are as follows:

Basic quantity	Estimated accuracy at M = 1.1	M = 0.87
W, percent	±0.5	±0.5
I_Z, percent	±2.0	±2.0
I_X, percent	±4.0	±4.0
I_{XZ}, percent	±9.0	±9.0
M, percent	±1.0	±1.7
q, percent	±2.0	±3.5
ω, percent	±2.5	±2.5
$\left\|\frac{\dot{\phi}}{\beta}\right\|$, percent	----	±3.0
$\left\|\frac{a_{t/g}}{\beta}\right\|$, percent	±2.0	±2.0
Ω_p, deg	----	±4
α, deg	±0.5	±0.5
a, sec^{-1}	±0.1	±0.1

The estimated maximum errors in these derivatives as a result of the errors given in this table were determined by the method used in reference 4. The accuracies are as follows: 3 to 8 percent for C_{Y_β}, 6 to 12 percent for C_{n_β} and C_{l_β}, and 15 to 25 percent for $C_{n_r} - C_{n_{\dot{\beta}}}$.

It is believed that the data presented in this report provide a good indication of how the lateral stability derivatives for this configuration vary with Mach number and that the absolute accuracy of these derivatives is as good as or better than indicated above.

ANALYSIS

A time history of the more significant quantities of the flight is presented in figure 4. Shown are angle of sideslip, roll rate, angle of attack, Mach number, and rudder deflection. The angle of sideslip curve shows typical damped oscillations at every change in control deflection, but the roll rate curve shows little effect of control deflection in the early part of the record. The roll builds up in rate to 3 radians per second at a Mach number of 0.94. Then the roll rapidly subsides.

The periods of the oscillations in angle of attack do not appear to be affected by coupling, since a comparison of these periods with those

of the model of reference 2 indicated the same variation of the location of the aerodynamic center.

The equations of motion used in the analysis of the lateral motions are as follows:

$$\frac{mV}{qS}\left(\dot{\beta} + r - \alpha p\right) = C_Y \tag{1}$$

$$\frac{I_X}{qSb}\dot{p} - \frac{I_{XZ}}{qSb}\dot{r} = C_{l_\beta}\beta + C_{l_p}\frac{pb}{2V} + \left(C_{l_r} - C_{l_{\dot{\beta}}}\right)\frac{rb}{2V} \tag{2}$$

$$\frac{I_Z}{qSb}\dot{r} - \frac{I_{XZ}}{qSb}\dot{p} = C_{n_\beta}\beta + C_{n_p}\frac{pb}{2V} + \left(C_{n_r} - C_{n_{\dot{\beta}}}\right)\frac{rb}{2V} \tag{3}$$

The terms shown in the simplified equations above were included on the basis of preliminary calculations and by consideration of the data available for analysis. These equations and the complete equations of the lateral mode are found in reference 4.

An estimation of the value of C_{n_p} indicated that it could be assumed to be zero for this test. The product-of-inertia terms also were zero, as indicated by measurements of the inclination of the principal axis.

The model motion has three modes: the spiral, the Dutch roll, and the highly damped roll modes. In tests as short as this one the spiral mode does not show up. The Dutch roll mode was analyzed by three-degree-of-freedom vector plots. The highly damped roll mode was analyzed as a one-degree-of-freedom system in roll. The logarithmic decrement of the mean roll rate represents the damping of this degree of freedom and is used in the solution of the roll damping derivative in the following equation, which is derived from the rolling moment equation by assuming $\beta = r = \dot{r} = 0$:

$$C_{l_p} = \frac{-0.693}{t_{0.5}}\frac{2VI_X}{qSb^2} \tag{4}$$

For the present test the oscillatory component of the rolling motion, which has the same frequency as the yaw motion, was very small, so that to a very good approximation it may be assumed zero and a two-degree-of-freedom solution used to obtain yawing-moment derivatives. The combination damping derivative is obtained from the side-force and yawing-moment equations as follows:

$$\left(C_{n_r} - C_{n_{\dot{\beta}}}\right) = \frac{2VI_Z}{qSb^2}\left(2a - \frac{C_{Y_\beta} qS}{mV}\right) \tag{5}$$

A single-degree-of-freedom equation of yawing moment was solved for C_{n_β} from the periods of the oscillations as follows:

$$C_{n_\beta} = \frac{I_Z}{qSb}\omega^2 \tag{6}$$

A three-degree-of-freedom analysis was carried out for three of the model oscillations in which the phase and amplitude relationships between the oscillatory components of rolling velocity and sideslip angle were reasonably discerned. These oscillations were analyzed by means of the vector method found in references 4 and 5. The amplitude ratio and phase angle of the roll rate, shown in figures 5 and 6, are the quantities whose lack prohibits the use of the time vector method of solution for other than these three oscillations.

The rudder hinge moment was measured by an instrument which indicated total hinge moment due to all causes. The variation of the moment coefficient per degree deflection $\frac{\Delta C_h}{\Delta\delta}$ was computed. The major component of hinge-moment coefficient not due to control deflection is $C_{h_\beta}\beta$, which was removed from the value of $\frac{\Delta C_h}{\Delta\delta}$ by using the hinge-moment coefficient values at the time when the angle of sideslip was zero. The change in hinge-moment coefficient per degree deflection found from these values provides a value of C_{h_δ} for comparison with the value described previously. The yawing-moment coefficient per degree rudder deflection was found by taking a ratio of change in trim angle of sideslip to change in rudder deflection and multiplying it by the yawing moment per degree sideslip, thus:

$$C_{n_\delta} = C_{n_\beta} \frac{\Delta\beta}{\Delta\delta} \tag{7}$$

The internal flow of the ducts was obtained from measurements of the total pressure before the choked exit of the duct. This method was explained in reference 2.

RESULTS

The range of Reynolds number based on wing mean aerodynamic chord and propeller windmilling speed for this test are shown as functions of Mach number in figures 7 and 8, respectively.

Figure 9 presents the supersonic values of duct mass-flow ratio at which this test was conducted. The amount of duct choking was designed to duplicate the inlet-velocity-ratio conditions of the full-scale airplane flying at $M = 0.94$ at approximately 20,000 feet.

Figures 10 and 11 show the frequency and damping, respectively, of the lateral oscillations. The curve of the damping factor is broken near a Mach number of 0.9 because the damping appeared to change in the unstable direction (see fig. 4), but there were an inadequate number of cycles present to determine what the damping was. There may have been either zero damping, an instability, or a brief disturbance.

The variation of lateral force with angle of sideslip is shown in figure 12 and the variation in slope of the lateral-force curve with Mach number is shown in figure 13. There is very little variation of C_{Y_β} with Mach number over the Mach number range covered by the test.

Using the information in figures 5, 6, and 10, the lateral-motion vector diagrams were plotted. The amplitude ratio of roll rate to sideslip angle in figure 5 shows points only when the motions in both roll rate and angle of sideslip were damped sinusoidal motions. The phase angle of roll rate to angle of sideslip (fig. 6) was found at the same Mach numbers. At other Mach numbers either or both of these quantities varied widely during the oscillation.

Shown in figure 14 is the time required for the mean roll rate to approach halfway to its final value, wherein the time is the damping information of the one-degree-of-freedom in roll. It can be seen in figure 4 that values for $t_{0.5}$ are difficult to determine because the natural period in yaw is nearly the same as $t_{0.5}$. The roll-damping

derivative C_{l_p} computed from this information is shown in figure 15. It is not known if the variation in C_{l_p} with Mach number is a trend or is an indication of inaccuracy in $t_{0.5}$. The use of the computed values of C_{l_p} in the rolling-moment vector diagrams enables the determination of the other two rolling-moment derivatives C_{l_β} and $C_{l_r} - C_{l_{\dot{\beta}}}$ (figs. 16 and 17).

The directional static stability derivative C_{n_β} presented in figure 18 was calculated from the periods of the lateral oscillations in addition to the vector diagram method. Excellent agreement is shown between the two methods of calculations. The variation of C_{n_β} with Mach number extended from a value of 0.25 at $M = 0.82$ to a value of 0.5 at $M = 1.11$.

The damping derivative $\left(C_{n_r} - C_{n_{\dot{\beta}}}\right)$ presented in figure 19 was also determined from the two-degree-of-freedom solution in addition to the vector diagram method.

The rudder effectiveness C_{n_δ} is shown in figure 20. It can be seen that the rudder is an effective control throughout the Mach number range covered by the test although the value of C_{n_δ} is reduced to about 43 percent of the subsonic value at speeds above $M = 0.9$.

The hinge-moment parameters $\frac{\Delta C_h}{\Delta \delta}$ and C_{h_δ} are presented in figure 21. The total hinge-moment parameter $\frac{\Delta C_h}{\Delta \delta}$ and C_{h_δ} agree quite well, particularly below $M = 0.85$ which indicates that the variation of C_h with β is small over the range of sideslip angles covered by this test.

CONCLUSIONS

Results from the flight test of a 0.133 scale model of the Convair XFY-1 airplane with windmilling propellers at Mach numbers from 0.71 to 1.12 indicate the following conclusions:

1. The static directional stability parameter varied somewhat with speed, being 0.25 at a Mach number of 0.82 and 0.5 at a Mach number of 1.11, with the center of gravity located at 13.9 percent mean aerodynamic chord.

2. The dynamic lateral stability, where found, although not invariant with speed, remained of the same magnitude in the stable direction throughout the flight.

3. The roll damping was good; a typical value of the damping-in-roll derivative was about -0.2.

4. The slope of the lateral-force curve varied little with speed, remaining about -1.9.

5. The yawing moment per degree deflection was about 0.28 subsonically and 0.12 supersonically.

Langley Aeronautical Laboratory,
National Advisory Committee for Aeronautics,
Langley Field, Va., October 24, 1955.

James A. Hollinger
Aeronautical Research Scientist

Grady L. Mitcham
Aeronautical Engineer

Approved: Joseph A. Shortal
Joseph A. Shortal
Chief of Pilotless Aircraft Research Division

rwh

REFERENCES

1. Hastings, Earl C., Jr., and Mitcham, Grady L.: Flight Determination of the Longitudinal Stability Characteristics of a 0.133-Scale Rocket-Powered Model of the Consolidated Vultee XFY-1 Airplane Without Propellers at Mach Numbers From 0.73 to 1.19 - TED No. NACA DE 369. NACA RM SL54B03a, Bur. Aero., 1954.

2. Hastings, Earl C., Jr., and Mitcham, Grady L.: Longitudinal Stability Characteristics of the Consolidated Vultee XFY-1 Airplane With Windmilling Propellers As Obtained From Flight of 0.133-Scale Rocket-Propelled Model at Mach Numbers From 0.70 to 1.13 - TED No. NACA DE 369. NACA RM SL54F11, Bur. Aero., 1954.

3. Sutton, Fred B., and Buell, Donald A.: The Effect of an Operating Propeller on the Aerodynamic Characteristics of a 1/10-Scale Model of the Lockheed XFV-1 Airplane at High Subsonic Speeds - TED No. NACA DE 377. NACA RM SA52E06, Bur. Aero., 1952. (Converted to NACA RM A52E06, 1954.)

4. Mitchell, Jesse L., and Peck, Robert F.: Investigation of the Lateral Stability Characteristics of the Douglas X-3 Configuration at Mach Numbers From 0.6 to 1.1 by Means of a Rocket-Propelled Model. NACA RM L54L20, 1955.

5. D'Aiutolo, Charles T., and Henning, Allen B.: Lateral Stability Characteristics at Low Lift Between Mach Numbers of 0.85 and 1.15 of a Rocket-Propelled Model of a Supersonic Airplane Configuration Having a Tapered Wing With Circular-Arc Sections and 40° Sweepback. NACA RM L55A31, 1955.

TABLE I.- PHYSICAL CHARACTERISTICS OF A 0.133-SCALE MODEL OF THE CONVAIR XFY-1 AIRPLANE

Wing:	
Area (included), sq ft	6.31
Theoretical span, ft	3.42
Aspect ratio (based on theoretical span)	1.85
Mean aerodynamic chord, ft	2.09
Sweepback of leading edge, deg	57
Sweepback of trailing edge, deg	9.25
Dihedral (relative to mean thickness line), deg	0
Taper ratio (Theoretical tip chord/Root chord)	0.22
Airfoil section	Modified NACA 63-009
Vertical tail:	
Area (included), sq ft	3.13
Span, ft	3.19
Aspect ratio	3.25
Sweepback of leading edge, deg	40
Sweepback of trailing edge, deg	6
Taper ratio (Theoretical tip chord/Root chord)	0.40
Airfoil section	Modified NACA 63-009
Elevon:	
Area (back of hinge line), sq ft	0.57
Chord (perpendicular to hinge line), ft	0.24
Span, ft	1.32
Propeller:	
Number of blades	6
Diameter, ft	2.14
Blade angle at 0.75 radius, deg	55
Airfoil section at 0.75 radius	NACA 65-707
Ducts:	
Inlet area of each duct, sq in	2.75
Exit area of each duct, sq in	1.77
Weight and balance:	
Weight, lb	208.8
Wing loading, lb/sq ft	33.1
Center-of-gravity location, percent $\bar{c}$	13.9
Moment of inertia in pitch, slug-ft^2	8.98
Moment of inertia in yaw, slug-ft^2	10.71
Moment of inertia in roll, slug-ft^2	1.76
Inclination of the principal axis, deg	0

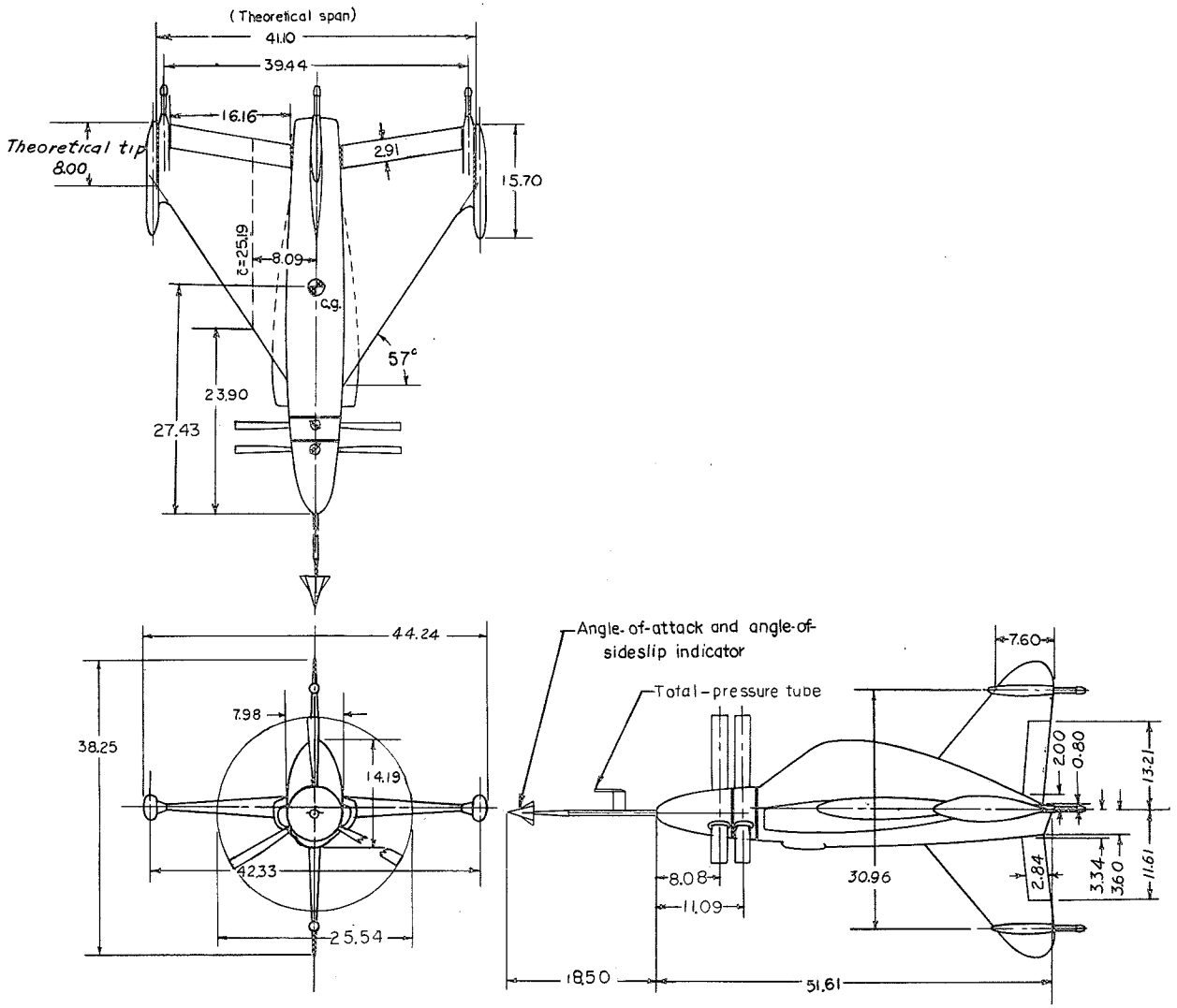

Figure 1.- Three-view drawing of the model. (All dimensions are in inches.)

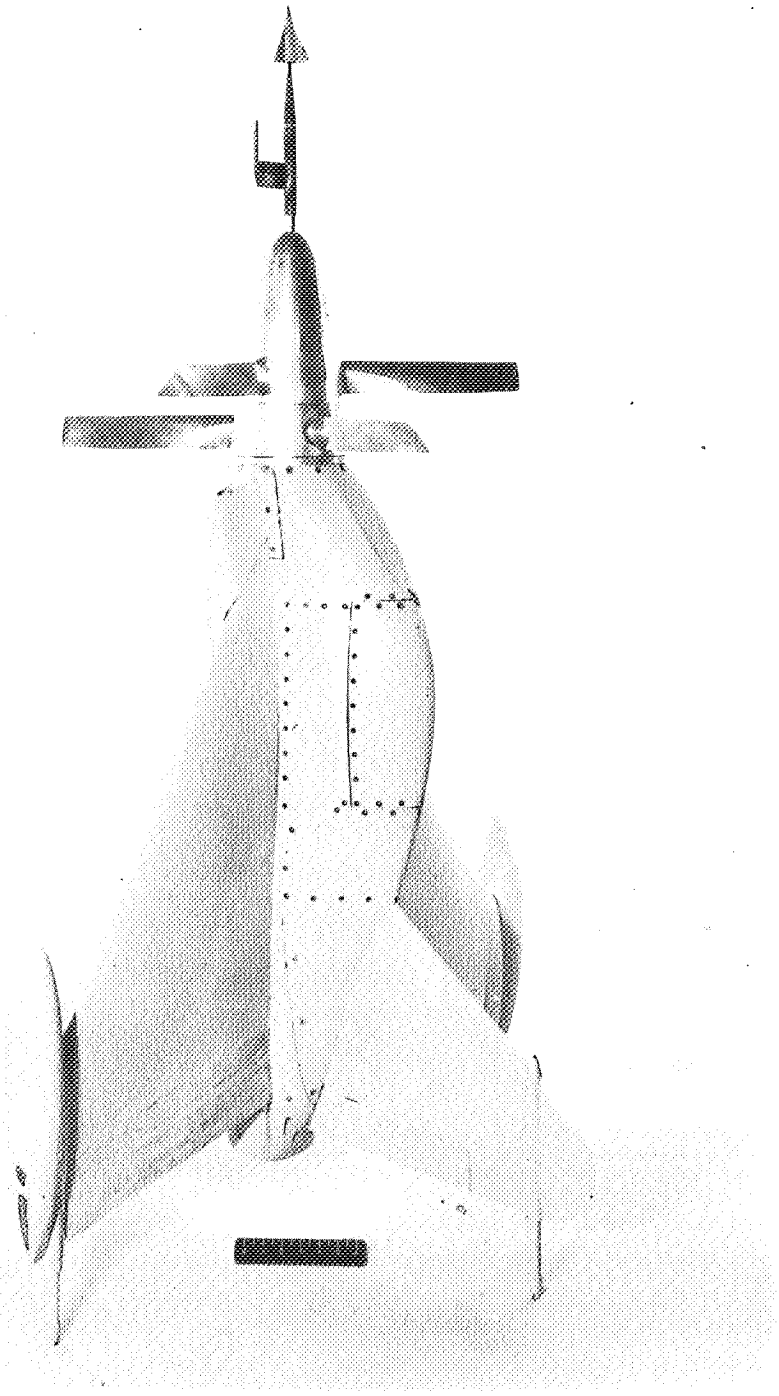

L-84754.1

(a) Free-flight rocket model.

Figure 2.- Photographs of the rocket model.

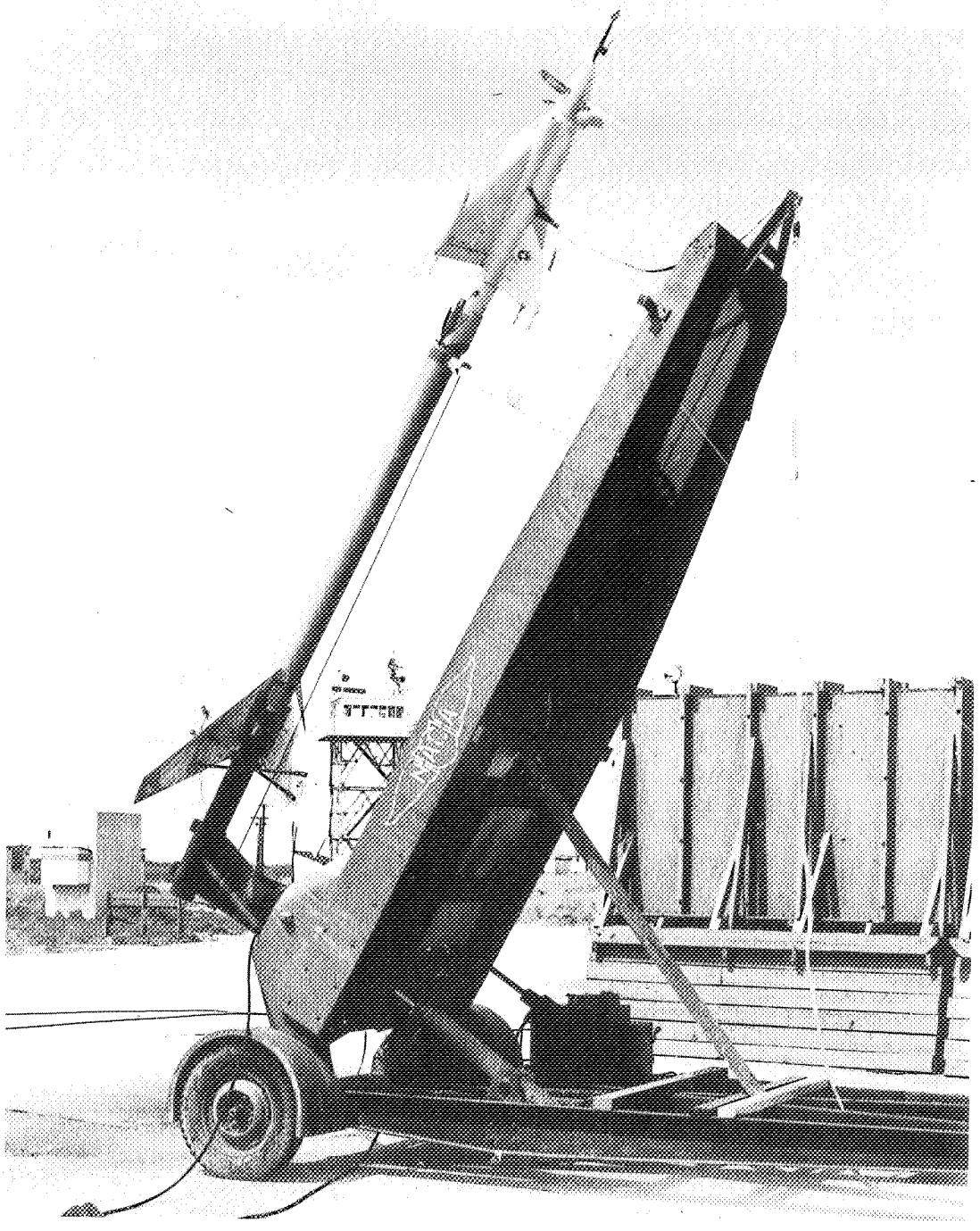

L-85037

(b) Booster-model combination on the launcher.

Figure 2.- Concluded.

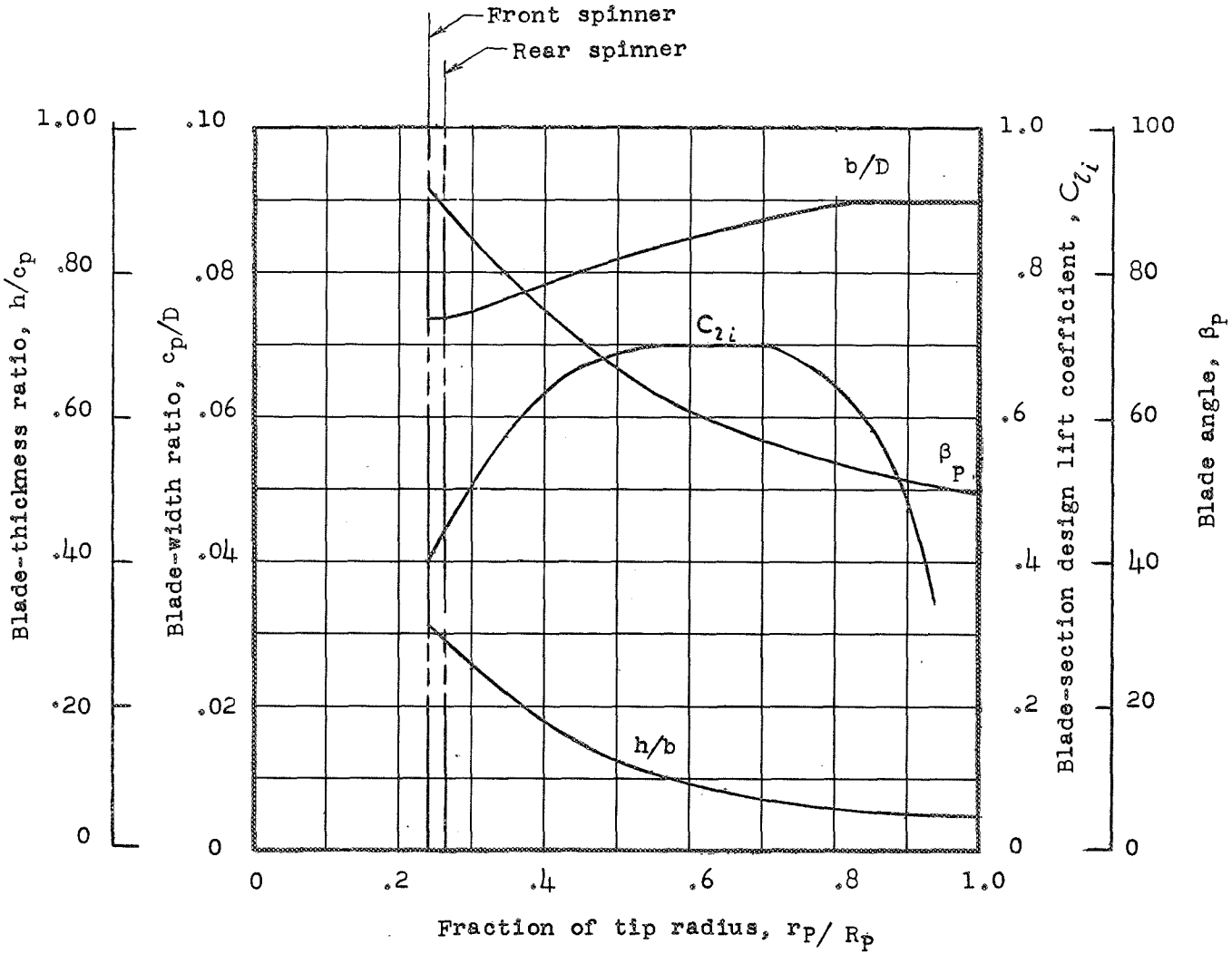

Figure 3.- Plan-form and blade-form curves for the Curtiss 1058-1059-XC4 dual-rotating propeller.

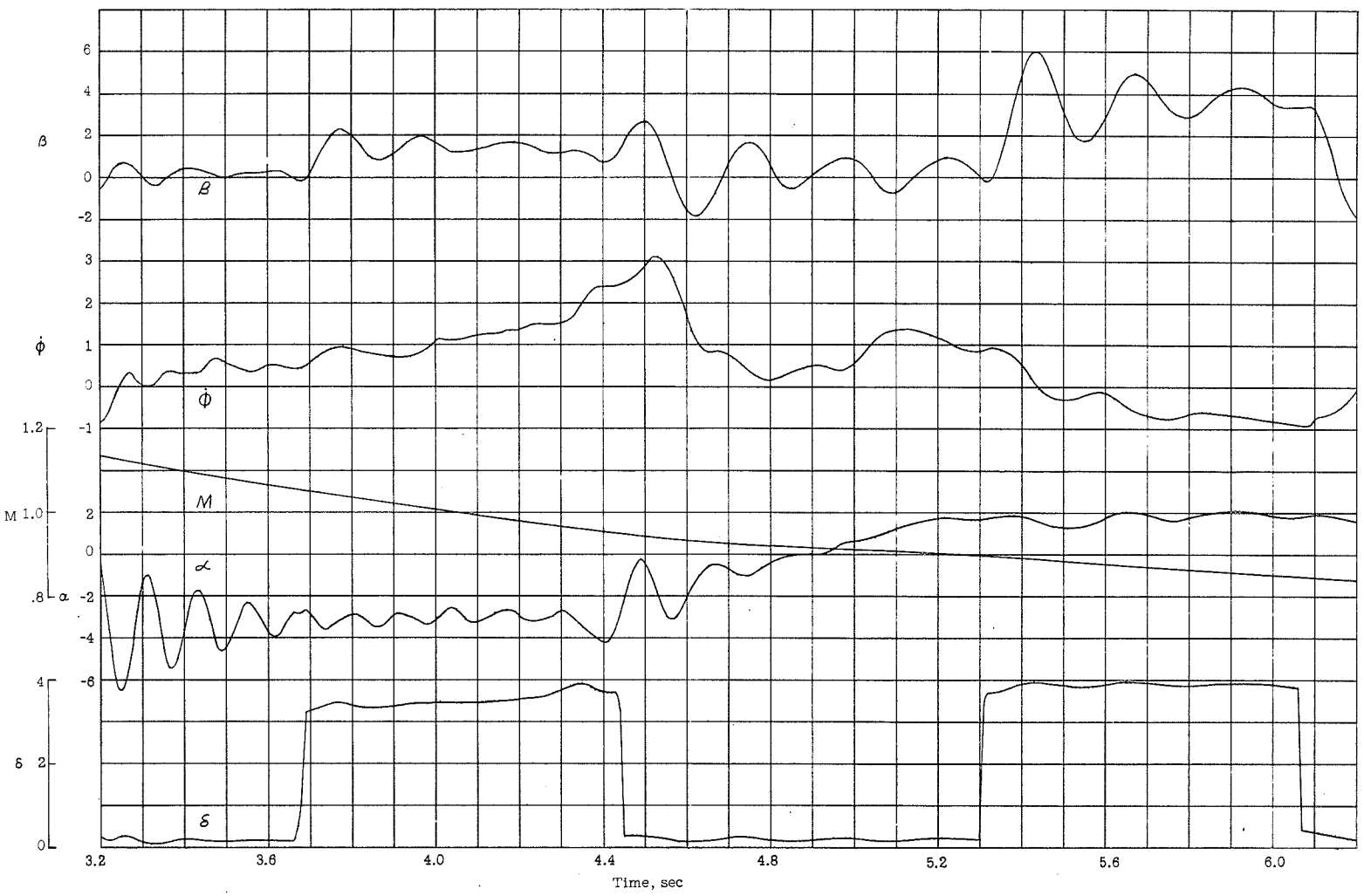

Figure 4.- Flight time histories of angle of attack, angle of sideslip, rate of roll, rudder deflection, and Mach number.

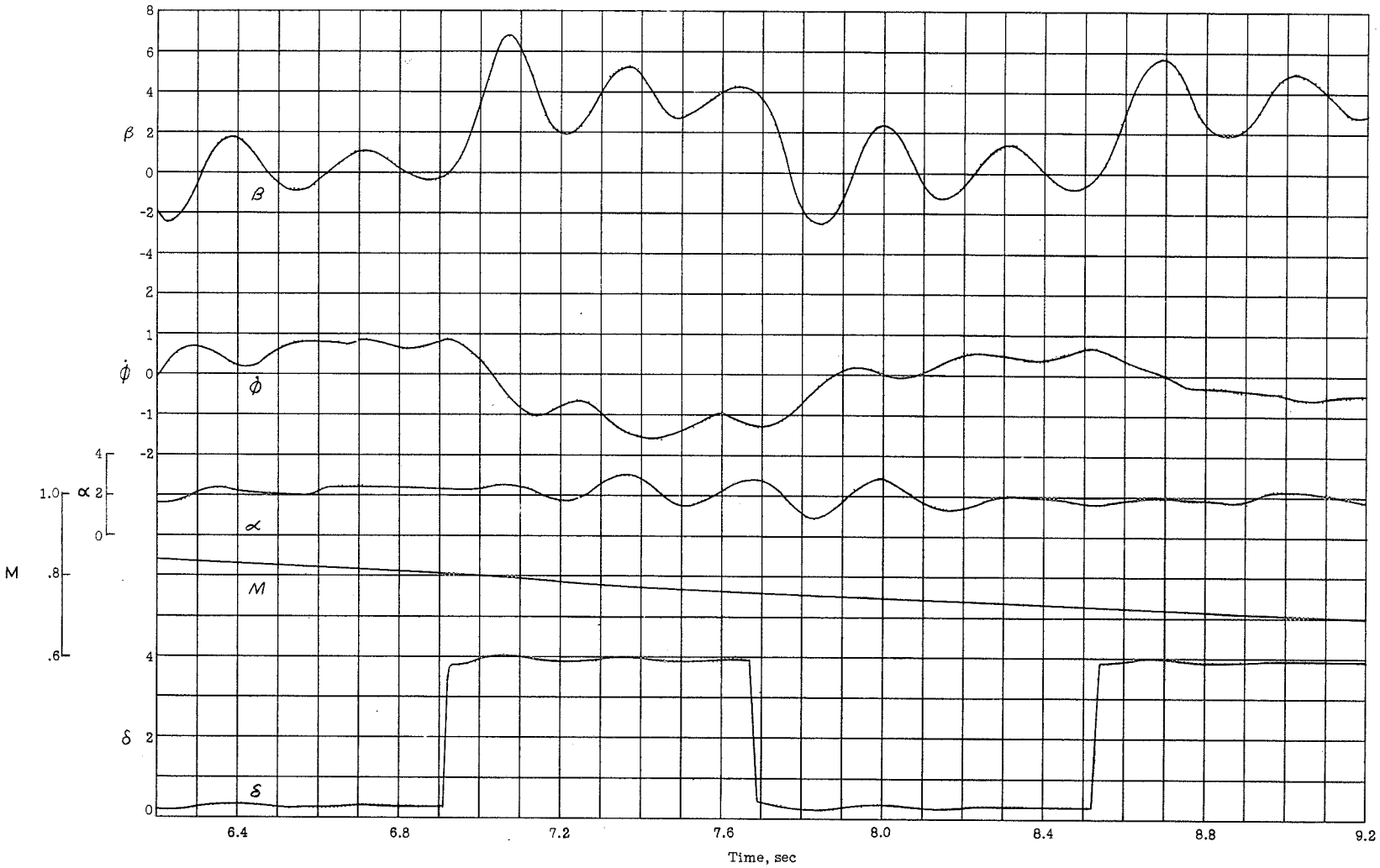

Figure 4.- Concluded.

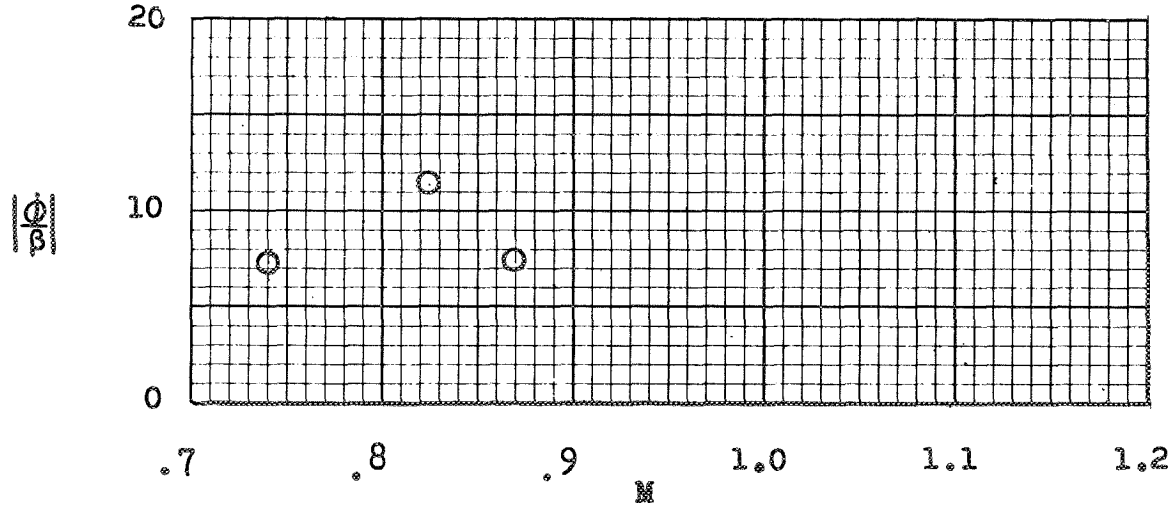

Figure 5.- Amplitude ratio in the lateral oscillation.

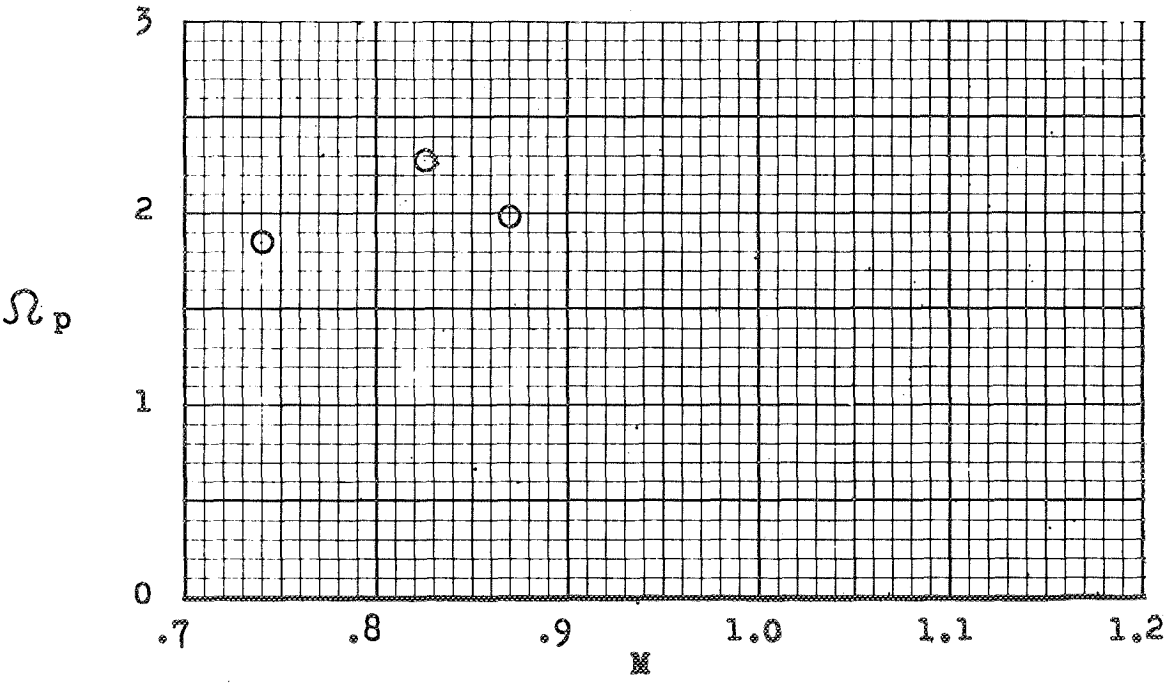

Figure 6.- Phase angle of rate of roll relative to angle of sideslip.

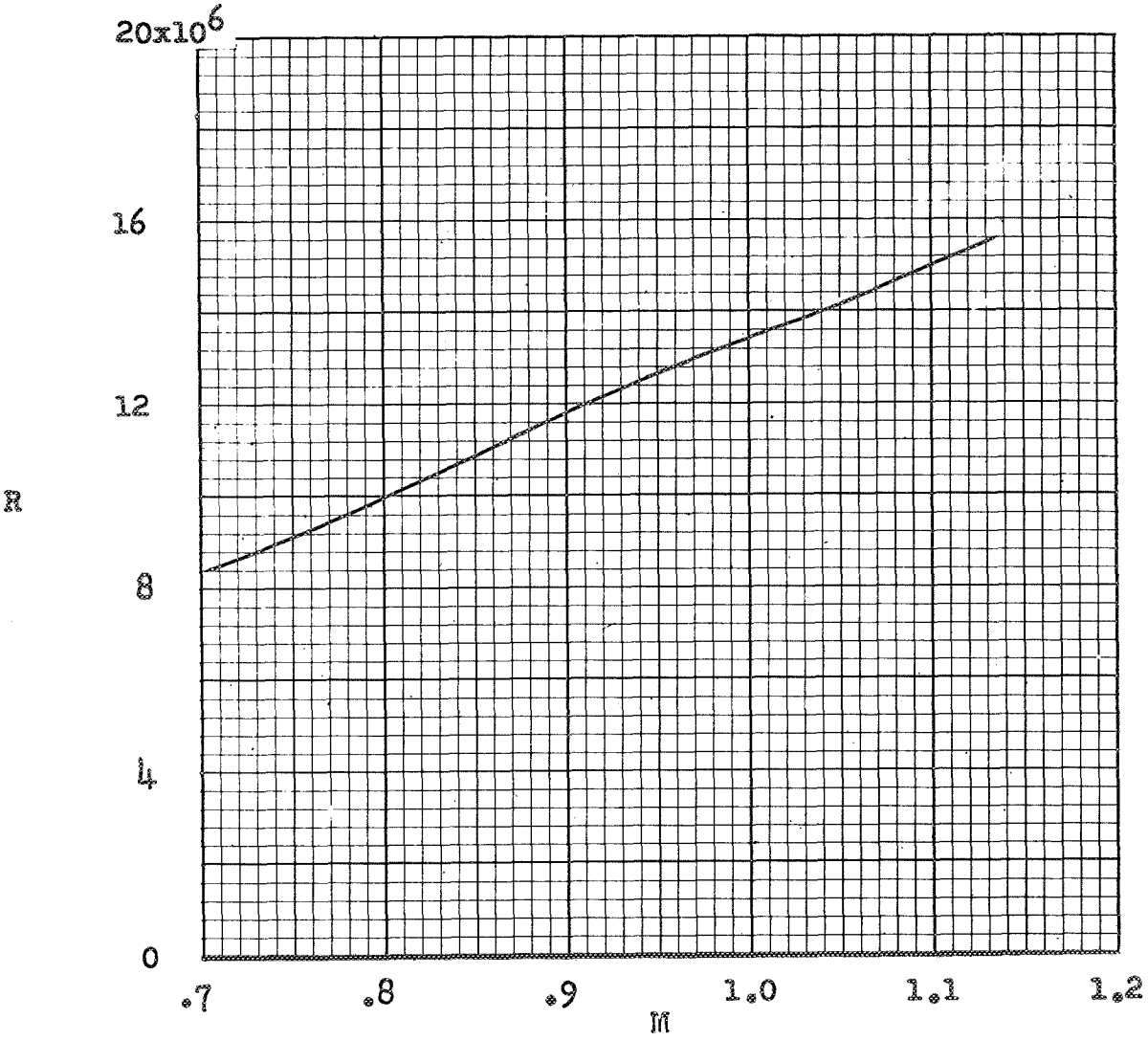

Figure 7.- Reynolds number based on wing mean aerodynamic chord as a function of Mach number.

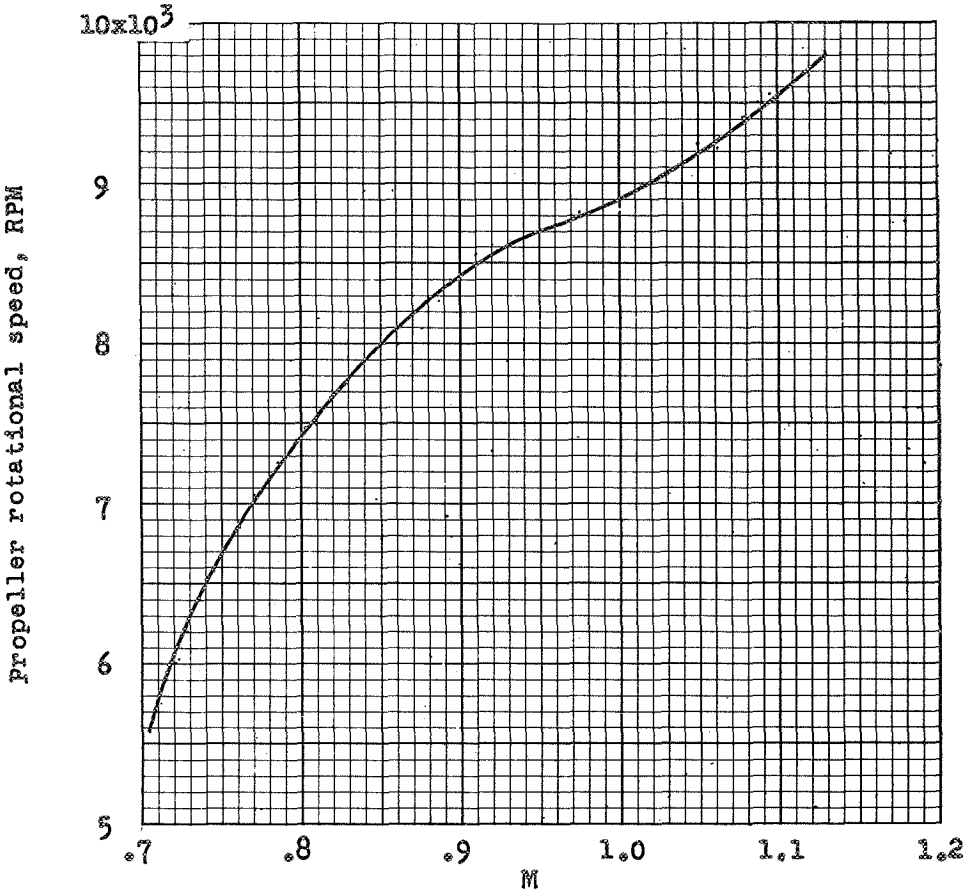

Figure 8.- Propeller windmilling speed as a function of Mach number.

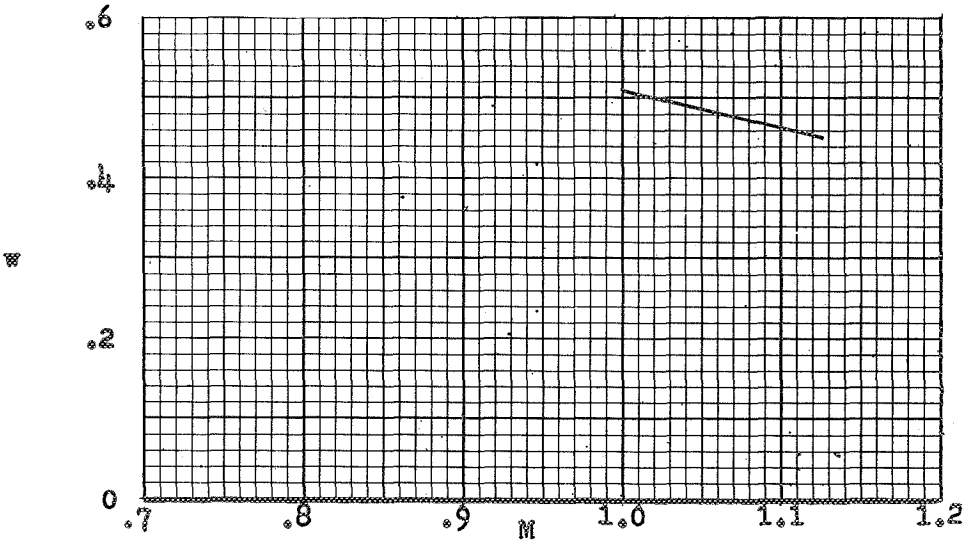

Figure 9.- Duct mass-flow ratio.

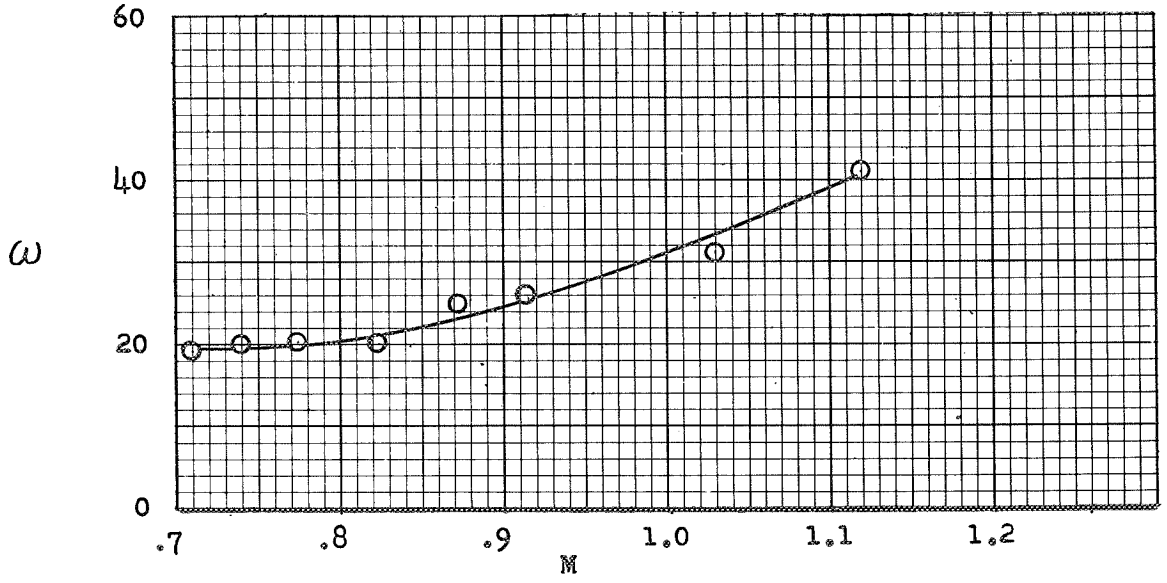

Figure 10.- Undamped natural circular frequency of Dutch roll oscillation.

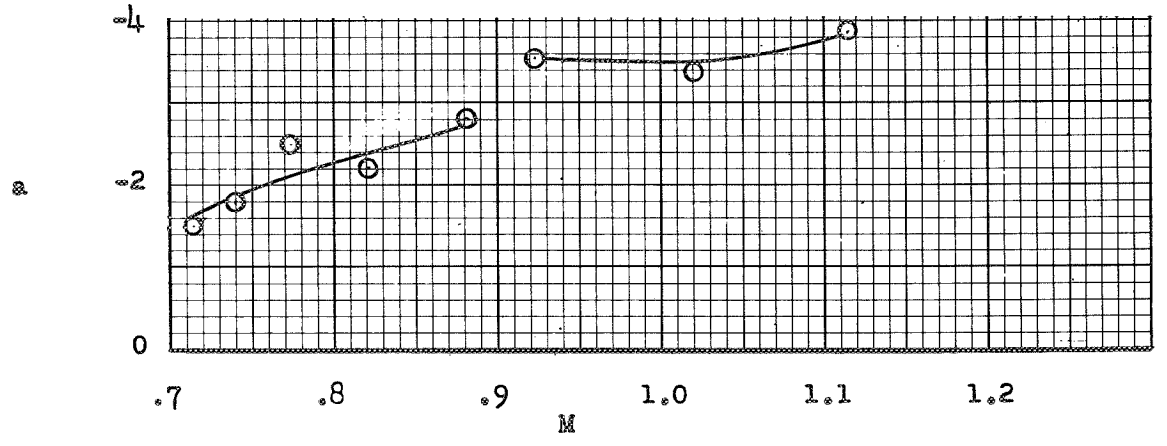

Figure 11.- Total damping factor of Dutch roll oscillation.

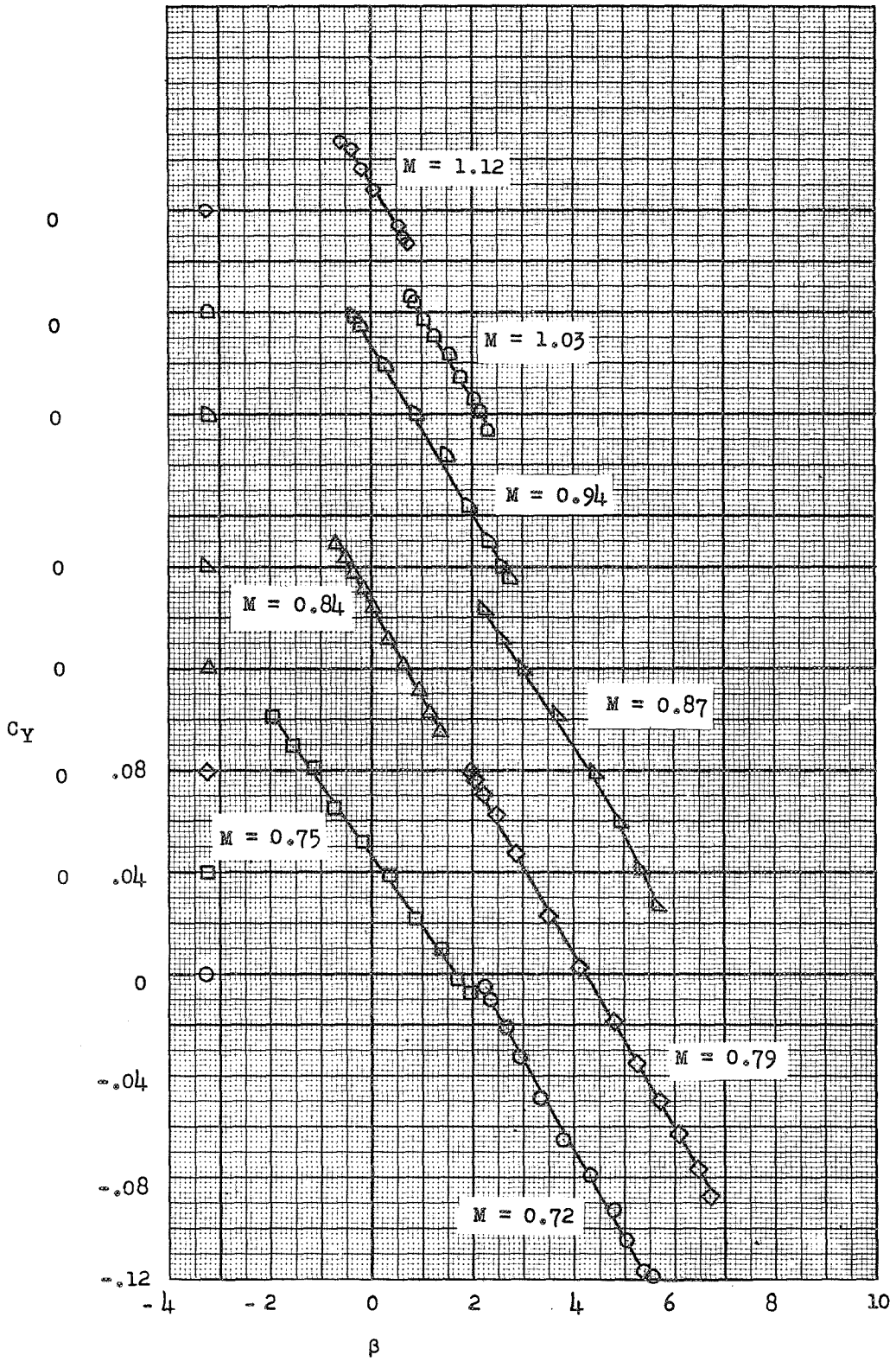

Figure 12.- Variation of lateral-force coefficient with angle of sideslip.

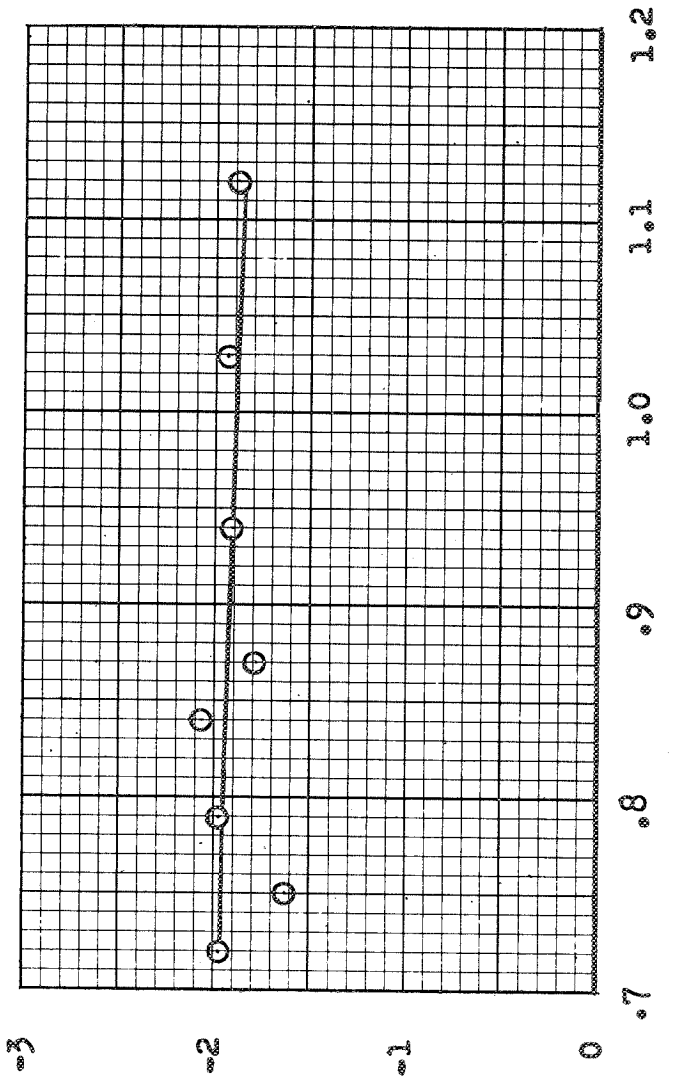

Figure 13.- Lateral-force derivative.

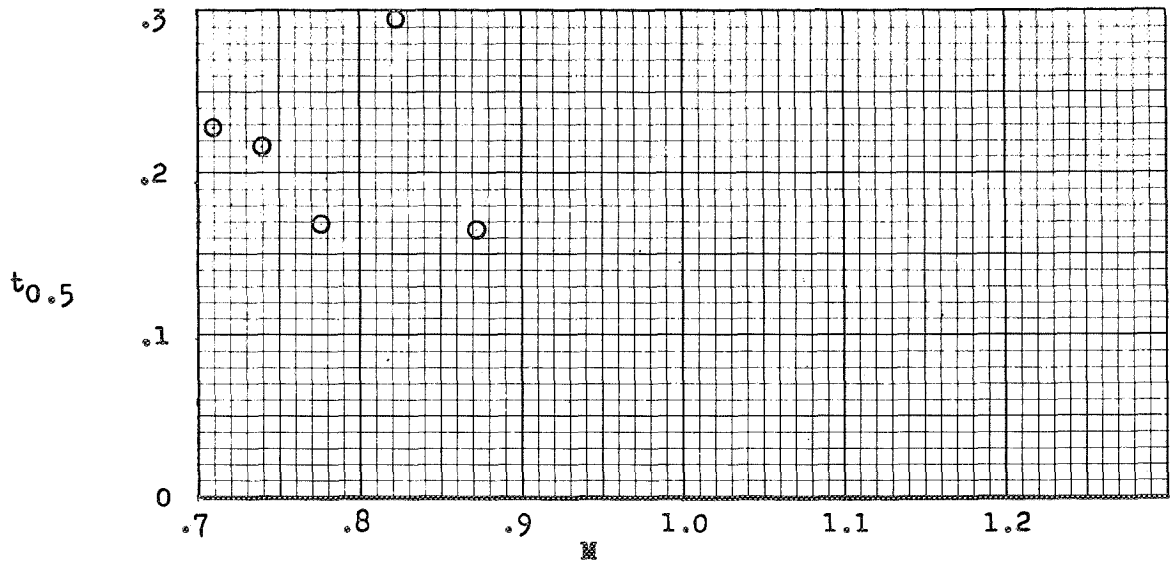

Figure 14.- Time required for mean roll rate to approach halfway to final value.

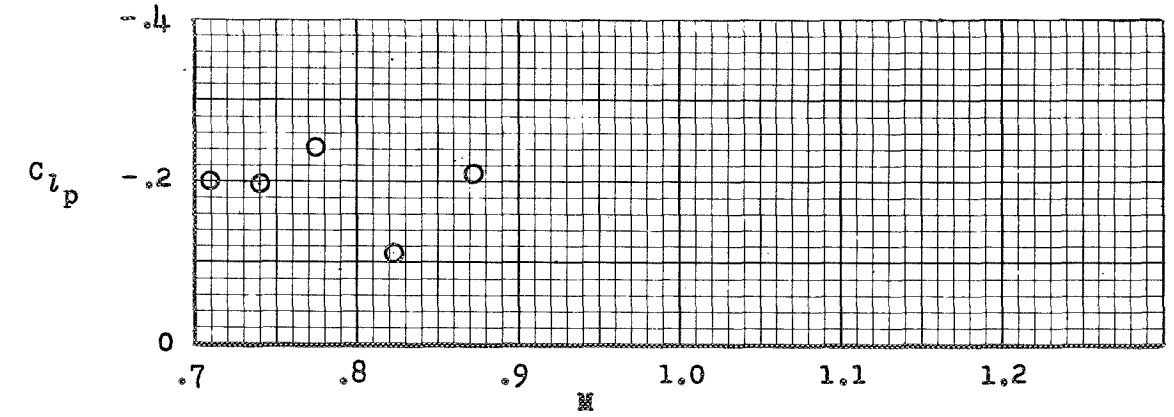

Figure 15.- Damping-in-roll derivative.

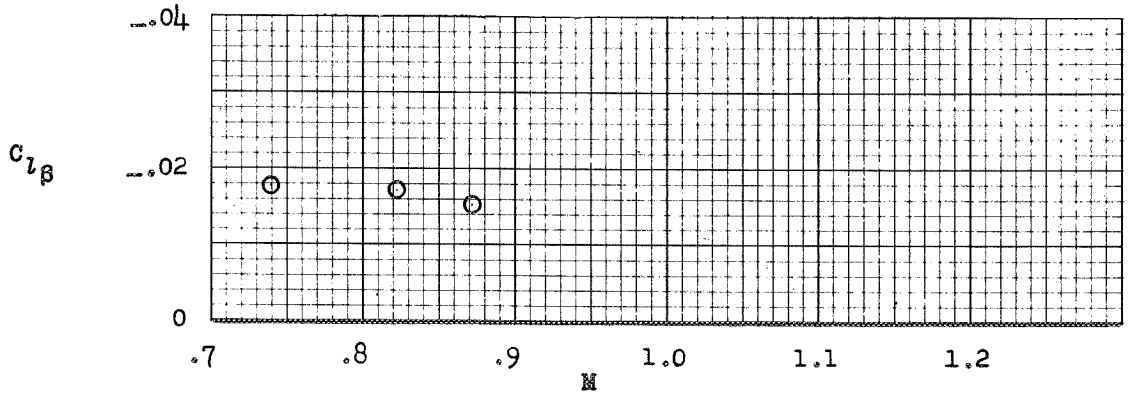

Figure 16.- Effective-dihedral derivative.

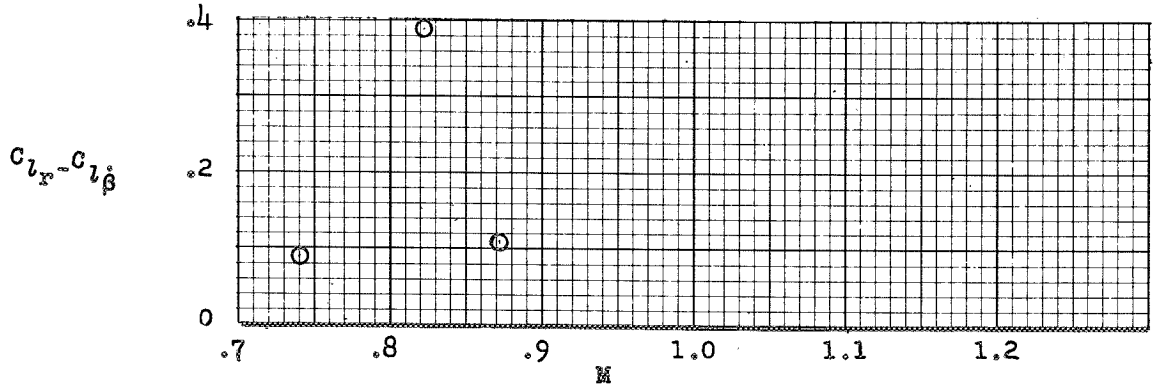

Figure 17.- Rolling-moment-due-to-yawing derivative.

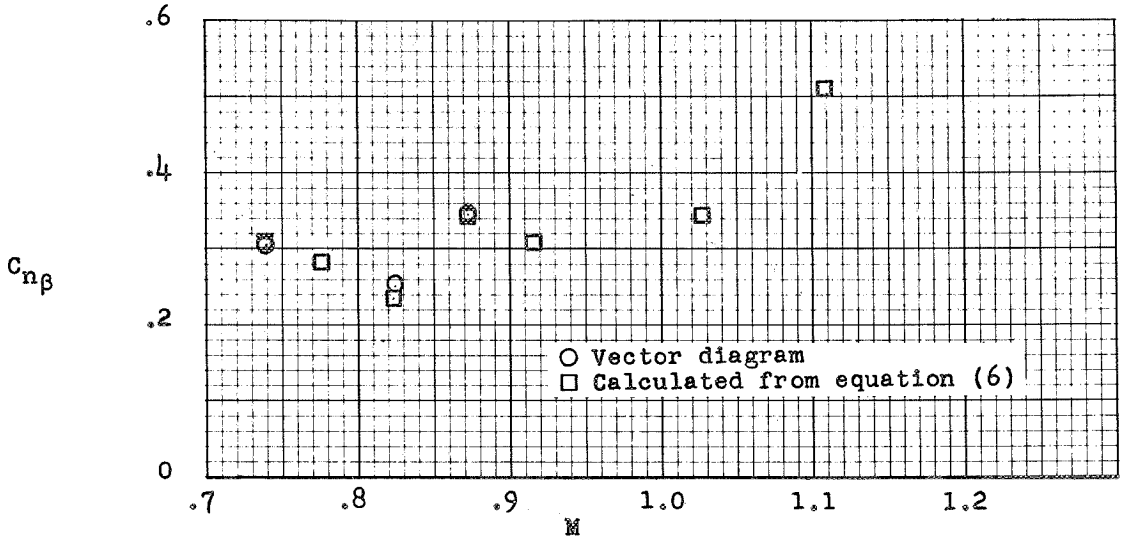

Figure 18.- Static-directional-stability derivative.

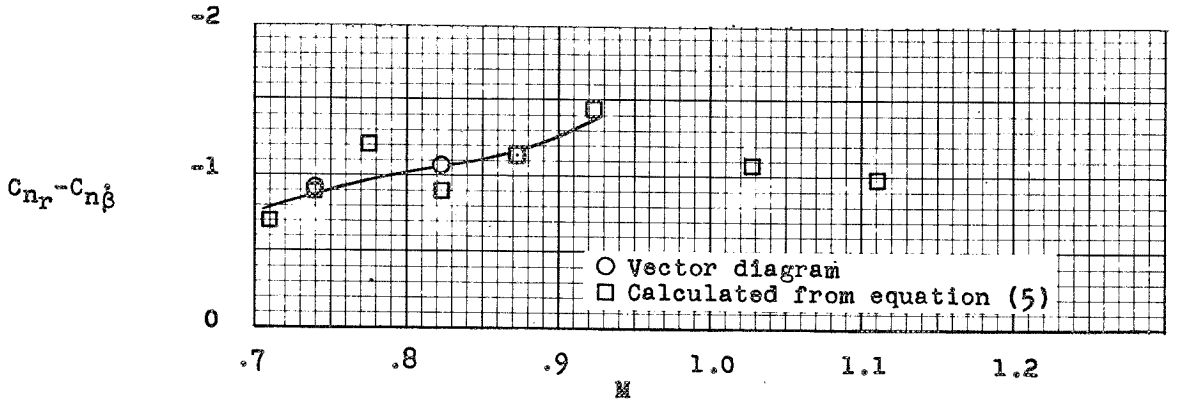

Figure 19.- Damping-in-yaw derivative.

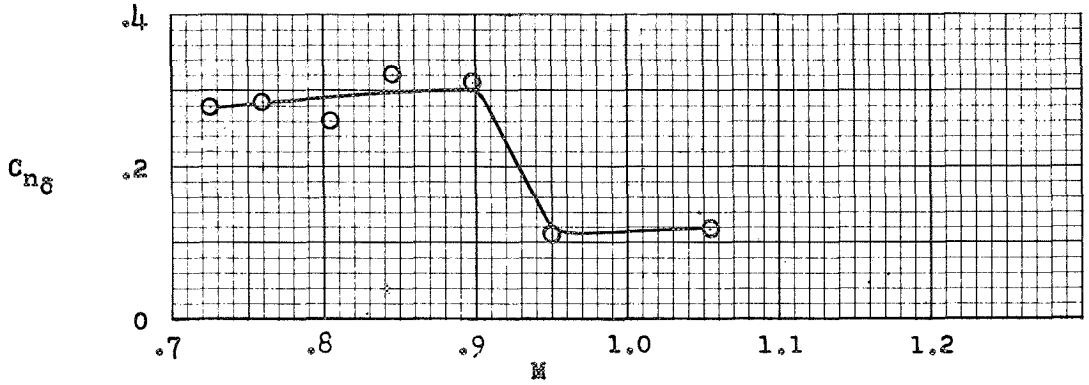

Figure 20.- Rudder effectiveness parameter.

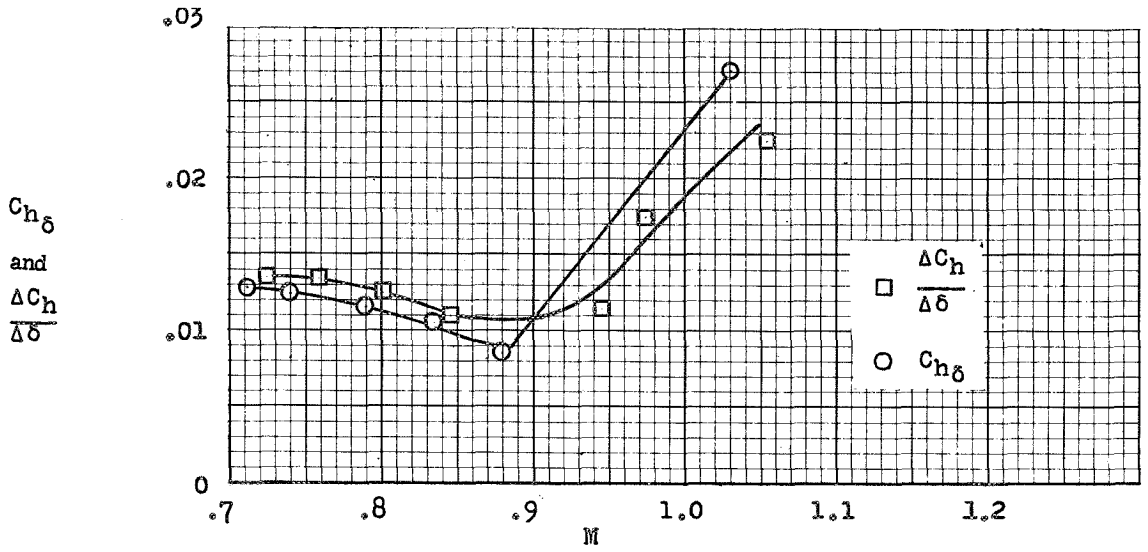

Figure 21.- Variation of hinge moment with rudder deflection.